# Biochar co-doped with nitrogen and boron switching the free radical based peroxydisulfate activation into the electron-transfer dominated nonradical process

Jibo Dou [a,b], Jie Cheng [a,b], Zhijiang Lu [c], Ziqi Tian [d], Jianming Xu [a,b], Yan He [a,b,*]

[a] Institute of Soil and Water Resources and Environmental Science, College of Environmental and Resource Sciences, Zhejiang University, Hangzhou 310058, China
[b] Zhejiang Provincial Key Laboratory of Agricultural Resources and Environment, Hangzhou 310058, China
[c] Department of Environmental Science and Geology, Wayne State University, Detroit, MI 48201, United States
[d] Ningbo Institute of Materials Technology and Engineering, Chinese Academy of Sciences, Ningbo 315201, China

## ARTICLE INFO

## ABSTRACT

In this study, N/B co-doped biochars were employed as metal-free activators of peroxydisulfate (PDS) for tetracycline degradation, more importantly, the roles of dopants and the relative contribution of radical vs nonradical oxidations were comprehensively investigated. Integrating with electron paramagnetic resonance and kinetics calculations, we showed that co-doping N and B into biochars not only boosted the catalytic activity but also switched the radical PDS-activated process into the electron transfer-dominated nonradical process. Compared with pristine biochar/PDS systems (22%), the nonradical contribution of N/B co-doped biochar/PDS systems increased to 59%, exhibiting outstanding stability and selectivity. Galvanic oxidation tests and theoretical simulations unveiled that doped biochars as conductive tunnels accelerate the potential difference-driven electron transfer from the highest occupied molecular orbital of pollutants to the lowest unoccupied molecular orbital of PDS due to the lower energy gap. This study provided new insights into the critical role of heteroatom-doped carbocatalysts in PDS nonradical activation.

## 1. Introduction

Carbonaceous materials-driven persulfate activation is emerging as a promising advanced oxidation process (AOP) for the green remediation of refractory organic contaminants. Diverse nanocarbon allotropes, such as carbon nanotubes (CNTs) and graphene, have been intensively exploited to catalyze persulfate, and the underlying mechanisms typically involve radical and nonradical pathways [1–3]. Despite the high oxidative potential, free radical-based oxidation is unselective, leading to insufficient degradation towards the target contaminants in complex environments [4]. Given that, a growing number of researchers have shifted their interests to the nonradical oxidation that exhibits high selectivity.

Heteroatom doping rises as a game-changer to modulate inherent electroactive sites of the parent carbon configuration, which not only render carbocatalysts a better catalytic efficacy but also is expected to trigger nonradical persulfate activation. Duan et al. discovered that

peroxymonosulfate (PMS) could be catalyzed by N-doped CNTs to form surface-confined reactive species, which attacked the organics by direct electron abstraction without producing free radicals [5]. A theoretical study by Liu et al. showed that the incorporated B atoms with a strong affinity toward peroxydisulfate (PDS) could act as Lewis acid sites to accelerate the mediated electron-transfer process [6]. Furthermore, Wang's group demonstrated that co-doping N and S also redistributed the spin and charge densities of CNTs, which could induce a higher catalytic activity towards PMS than the single-doped one [7]. Despite these advances, the mechanistic roles of dopants in the nonradical persulfate activation remain obscure. Especially, most studies lack quantitative analysis to distinguish the effects of dopants on the radical and nonradical pathways. In addition, the high operational cost of nanocarbon-based systems currently impedes their scale applications.

Compared with those expensive nanocarbons, biochar shows great advantages owing to its easily available raw materials and tunable structure, and it has become an industrially and economically attractive

carbocatalyst [8,9]. Zhu et al. first found that a nonradical pathway (singlet oxygenation and surface-confined complex) emerged and dominated the oxidation process in the N-doped graphitic biochars/PDS system [10]. Subsequently, Ho and co-workers further proposed that the surface reactive complexes on the N-doped BC were similar to that on the N-doped CNTs [11]. To date, lots of non-radical mechanisms and calculations were constructed on the low-dimensional nano-carbon-based systems [12–14]. However, these theoretical bases still need to be investigated in the high-dimensional carbocatalysts (e.g., biochar) that possess more complicated structures. Collectively, from the perspective of techno-economics, an improved understanding regarding the nature of dopants in the biochar-catalyzed persulfate system is of significance to the rational design of reaction-targeted carbocatalysts for persulfate-AOPs.

In this work, tetracycline (TC) was selected as the target compound due to its widespread in environments and inefficient removal by conventional treatment technologies [15]. We aim to (1) prepare a series of biochar samples doped with different N and B contents and unveil the roles of dopants in PDS activation for TC degradation; (2) identify the reactive species and oxidation pathways through a comprehensive analysis of radical quenching, electron paramagnetic resonance (EPR) studies, electrochemical tests, and in situ Raman observation, with a special interest for disclosing the mysteries behind the electron-transfer pathway on a basis of in-depth illustration regarding the potential difference.
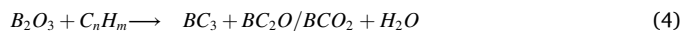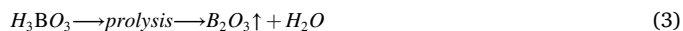
## 2. Materials and methods

### 2.1. Chemicals

Sodium persulfate ($Na_2S_2O_8$, Aladdin) was selected as the oxidizer because of the lower O-O bond dissociation energy (140 kJ mol$^{-1}$ for PDS and 213.3 kJ mol$^{-1}$ for PMS) and lower price [16]. Tetracycline (TC), 2,4,6-trichloropheol (TCP), phenanthrene (PHE), 5,5-dimethyl-1--pyrroline N-oxide (DMPO), 2,2,6,6-tetramethyl-4-piperidinol (TEMP), nitrobenzene (NB), benzoic acid (BA), and p-benzoquinone (p-BQ) were all provided from Aladdin Industrial Co., Ltd. (Shanghai, China). Methanol (MeOH), tert-butyl alcohol (TBA), furfuryl alcohol (FFA), and deuterium oxide ($D_2O$) were purchased from Macklin Biochemical Co., Ltd (Shanghai, China). Artificial surface water was prepared according to the previous literature [17]. The municipal wastewater sample was collected from a wastewater treatment plant in Xi'an, China. Following this, 30 mg of TC was spiked into the wastewater samples. The detailed composition of water samples was described in the Supporting Information, Table S1.

### 2.2. Synthesis and characterizations of biochars

The doped biochars were synthesized based on a slightly modified method [12]. In brief, wheat straw powder (1 g, 80 mesh) and urea (1, 2, 3 g) were mixed in 50 mL water and stirred at 70 °C to evaporate the solvent. After grinding, the dried powder was then transferred into a tube furnace and pyrolyzed at 700 °C under a flowing $N_2$ for 1 h with a ramping rate of 10 °C min$^{-1}$. The products were denoted as BC-N-1, BC-N-2, BC-N-3, respectively. N/B co-doped biochars were prepared by pyrolyzing a mixture of the presynthesized N-doped biochars (2 g) and boric acid (1 g) at 700 °C for 1 h. The final products were rinsed with boiling water [13], grounded, and denoted as BC-NB-1. BC-NB-2 and BC-NB-3, respectively. For comparison, the pristine biochar was prepared via the same procedure except for adding urea and boric acid.

Urea was decomposed and boric acid was dehydrated to afford N and B sources, respectively. The formation of C-N and C-B bonds is as follows (Eqs. (1–4)) [18]:

$$CO(NH_2)_2 \longrightarrow prolysis \longrightarrow NH_3\uparrow + HCNO \tag{1}$$

$$NH_3 + C_nH_m \longrightarrow C_xN_y \tag{2}$$

$$H_3BO_3 \longrightarrow prolysis \longrightarrow B_2O_3\uparrow + H_2O \tag{3}$$

$$B_2O_3 + C_nH_m \longrightarrow \quad BC_3 + BC_2O/BCO_2 + H_2O \tag{4}$$

The as-prepared samples were characterized by scanning electron microscope (SEM), energy-dispersive X-ray spectroscopy (EDX), $N_2$ adsorption/desorption apparatus, elemental analyzer, Raman, Fourier transform infrared spectroscopy (FTIR), and X-ray photoelectron spectroscopy (XPS). Detailed information is available in Text S1.

### 2.3. Batch experiments

In a typical experiment, 20 mg of biochar was dispersed in 100 mL of contaminant solution ($[TC]_0 = 30$ mg L$^{-1}$), then the reaction was initiated by adding 1 mM of PDS. The solution pH was not adjusted unless otherwise stated. The sample was withdrawn at given intervals, filtered through a 0.22-μm PTFE filter, and mixed with MeOH ($V_{sample}$: $V_{MeOH} = 1$: 1) for concentration measurement. After reactions, biochars were recovered by centrifugation and rinsed with ultrapure water and ethanol.

The observed rate constant ($k_{obs}$, min$^{-1}$) of TC degradation was calculated by the pseudo-first-order kinetics model (Eq. (5)) [19]. Competition kinetics experiments were conducted by using NB and BA as probe compounds to estimate the steady-state concentrations of radicals (Eqs. (6, 7)) [9]. The relative contributions of $^\bullet OH$, $SO_4^{\bullet-}$, and nonradical oxidation are calculated according to Eqs. (8–11) [9]. Also note that the oxidative degradation of pollutants was obtained by subtracting the adsorption contribution from the overall removal of pollutants at different time intervals. Additionally, the conclusion of oxidation contribution was further verified by TCP degradation using the same method. Detailed kinetics calculations are shown in Text S2.

$$\ln([TC]/[TC]_0) = \quad -k_{obs}t \tag{5}$$

$$\ln([NB]/[NB]_0) = \quad -k_{\bullet OH,NB}[\bullet OH]_{ss}t \quad = -k_{obs,NB}t \tag{6}$$

$$\ln([BA]/[BA]_0) = \quad -(k_{\bullet OH,BA}[\bullet OH]_{ss} + k_{SO4\bullet-,BA}[SO_4^{\bullet-}]_{ss})t \quad = -k_{obs,BA}t \tag{7}$$

$$\ln([TC]/[TC]_0) = \quad -k_{obs,TC}t \tag{8}$$

$$R_{\bullet OH} = (k_{\bullet OH,TC}[\bullet OH]_{ss})/k_{obs,TC} \tag{9}$$

$$R_{SO4\bullet-} = (k_{SO4\bullet-,TC}[SO_4^{\bullet-}]_{ss})/k_{obs,TC} \tag{10}$$

$$R_{nonradical} = 1 - R_{\bullet OH} - R_{SO4\bullet-} \tag{11}$$

where $[NB]_0$, $[BA]_0$, and $[TC]_0$ represent the initial concentrations of NB, BA, and TC, respectively; $[NB]$, $[BA]$, and $[TC]$ represent the concentrations of NB, BA, and TC at a given reaction time, respectively; $[^\bullet OH]_{ss}$ and $[SO_4^{\bullet-}]_{ss}$ are the steady-state concentrations of $^\bullet OH$ and $SO_4^{\bullet-}$, respectively; $k_{\bullet OH, NB}$ is the second-order rate constants of $^\bullet OH$ with NB; $k_{\bullet OH, BA}$, $k_{SO4\bullet-, BA}$, $k_{\bullet OH, TC}$, $k_{SO4\bullet-, TC}$ are the second-order rate constants of $^\bullet OH$ and $SO_4^{\bullet-}$ with BA and TC, respectively; $k_{obs, NB}$, $k_{obs, BA}$, and $k_{obs, TC}$ are the pseudo-first-order rate constants of NB, BA, and TC, respectively; $R_{\bullet OH}$, $R_{SO4\bullet-}$ and $R_{nonradical}$ are the relative contribution of $^\bullet OH$, and $SO_4^{\bullet-}$, nonradical oxidation, respectively.

Quenching experiments of $SO_4^{\bullet-}$ and $^\bullet OH$ was carried out using MeOH and TBA as radical scavengers, respectively. FFA and p-BQ were used to quench $^1O_2$ and superoxide anion radical ($^\bullet O_2^-$), respectively. To directly verify the electron-transfer process, the catalyst was coated onto a graphite electrode and a two-chamber galvanic oxidation reactor was developed to separate the organic contaminants from PDS. Detailed experimental procedures are shown in Text S3. Furthermore,
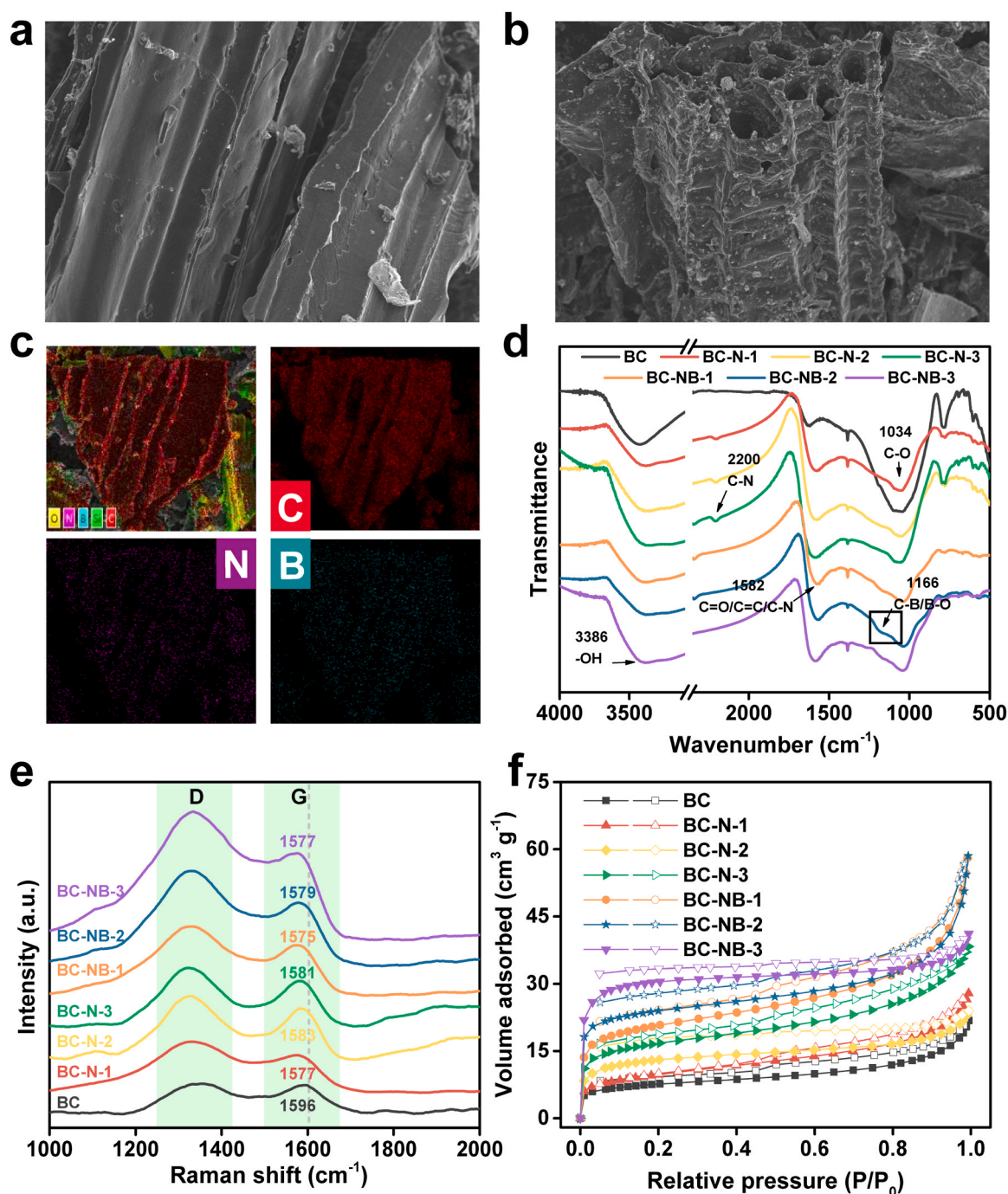
**Fig. 1.** SEM images of (a) pristine biochar and (b) BC-NB-1; (c) EDS mapping of BC-NB-1. (d) FTIR spectra, (e) Raman spectra, and (f) $N_2$ adsorption-desorption isotherms of biochars.

degradation experiments of TC, TCP, and PHE (1 mg $L^{-1}$) were performed to validate the assumption of potential energy difference-driven electron transfer pathway.

### 2.4. Analytical methods

The concentration of TC was quantified by an ACQUITY-class ultra-high performance liquid chromatography coupled with a TQ-XS tandem mass spectrometer (UPLC/MS/MS) (Waters, Milford, MA), equipped with a C18 reverse-phase column (Waters, 100 mm * 2.1 mm, 1.7 μm) and a UV detector. Total organic carbon (TOC) analysis was completed using a Multi 3100 TOC analyzer (JENA Co., Ltd., German). Sulfate ions

($SO_4^{2-}$) were determined by a Dionex ICS-2000 ion chromatography instrument. Free radicals ($SO_4^{\bullet-}$, $^{\bullet}OH$, and $O_2^{\bullet-}$) and $^1O_2$ were identified by a Bruker ESRA-300 electron paramagnetic resonance spectrometer at room temperature by using DMPO and TEMP as spin trapping agents, respectively. The electrochemical experiments, including linear sweep voltammetry, chronoamperometry, and electrochemical impedance spectroscopy (EIS), were performed on a Bio-logic VMP3 electrochemical workstation. The first principles were employed to perform by Vienna Ab initio Simulation Package with the projector augmented wave (PAW) method [20–22]. The structure of $O_8S_2$ and organic pollutants were optimized by the Gaussian software at the ωB97XD/def2-SVP level [23,24]. More details for analyses of pollutant

**Table 1**
$S_{BET}$, $I_D/I_G$ values, and elemental content of different biochars.

| | Pristine biochar | BC-N-1 | BC-N-2 | BC-N-3 | BC-NB-1 | BC-NB-2 | BC-NB-3 | Used BC-NB-1 | Recycled BC-NB-1 |
|---|---|---|---|---|---|---|---|---|---|
| $S_{BET}$ (m$^2$ g$^{-1}$) | 26.74 | 34.71 | 45.49 | 58.29 | 72.01 | 92.61 | 103.47 | – | – |
| $I_D/I_G$ | 1.087 | 1.106 | 1.172 | 1.194 | 1.214 | 1.251 | 1.288 | – | – |
| C (wt%) | 52.10 | 56.27 | 53.93 | 54.18 | 56.78 | 55.95 | 54.48 | – | – |
| H (wt%) | 1.75 | 1.74 | 1.57 | 1.56 | 1.87 | 1.81 | 5.71 | – | – |
| N (wt%) | 0.75 | 8.32 | 11.86 | 15.84 | 8.62 | 11.41 | 14.05 | – | – |
| S (wt%) | 0.17 | 0.05 | 0 | 0 | 0.05 | 0 | 0 | – | – |
| C 1s (at%) | 81.71 | 75.00 | 74.12 | 72.62 | 68.62 | 64.30 | 64.86 | 67.14 | 73.09 |
| O 1s (at%) | 16.38 | 12.84 | 12.96 | 10.35 | 19.36 | 19.32 | 15.66 | 22.47 | 15.18 |
| N 1s (at%) | 1.91 | 12.16 | 12.92 | 17.03 | 10.22 | 14.58 | 17.58 | 9.43 | 9.89 |
| B 1s (at%) | – | – | – | – | 1.80 | 1.80 | 1.90 | 0.95 | 1.84 |
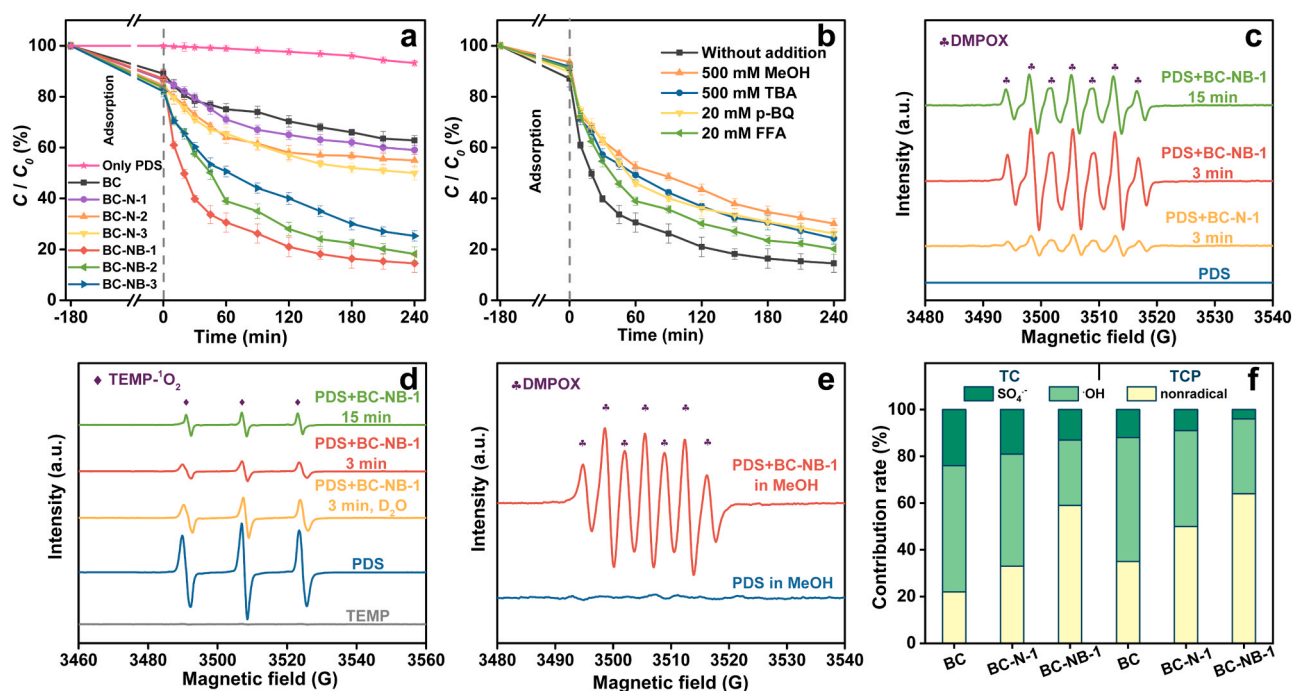


**Fig. 2.** (a) TC degradation in different systems; (b) quenching experiments in the BC-NB-1/PDS system; EPR spectra were obtained with the addition of (c, e) DMPO and (d) TEMP under different systems. (f) The contributions of radical and nonradical pathways.

quantification, EPR measurements, electrochemical tests, in situ Raman, and theoretical calculations are presented in Text S4–8.

## 3. Results and discussion

### 3.1. Characterization of biochars

As shown in the SEM images (Fig. 1a, b), compared with the smooth and flake structure of pristine biochar, the surface becomes rough and porous after modification. This can be attributed to the volatilization of urea to create a richer porous structure [25]. EDS mapping of BC-NB-1 further indicated the presence of N and B atoms, which were distributed uniformly in the biochar skeleton (Fig. 1c). A new band centered at 2200 cm$^{-1}$ representing C-N was observed in FTIR spectra, suggesting the successful incorporation of N atoms (Fig. 1d). Moreover, after being treated with boric acid, a weak band at 1166 cm$^{-1}$ was associated with the C-B/B-O bonds vibration, validating the existence of B atoms [26, 27]. The elemental composition of biochars was further measured by ultimate analysis and XPS. The results revealed that the contents of N in the doped biochars were much higher than that of the pristine biochar (Fig. S1, Table 1). As expected, the N content of doped biochars had a positive relationship with the urea addition, demonstrating that this modification method can well control the level of nitrogen doping (Fig. S2). Also, we observed a remarkable increase in the B content for the boric acid-treated biochars compared to the pristine biochar and N-doped ones (Fig. S1, Table 1). The above results together confirmed the successful incorporation of N and B atoms into the biochars.
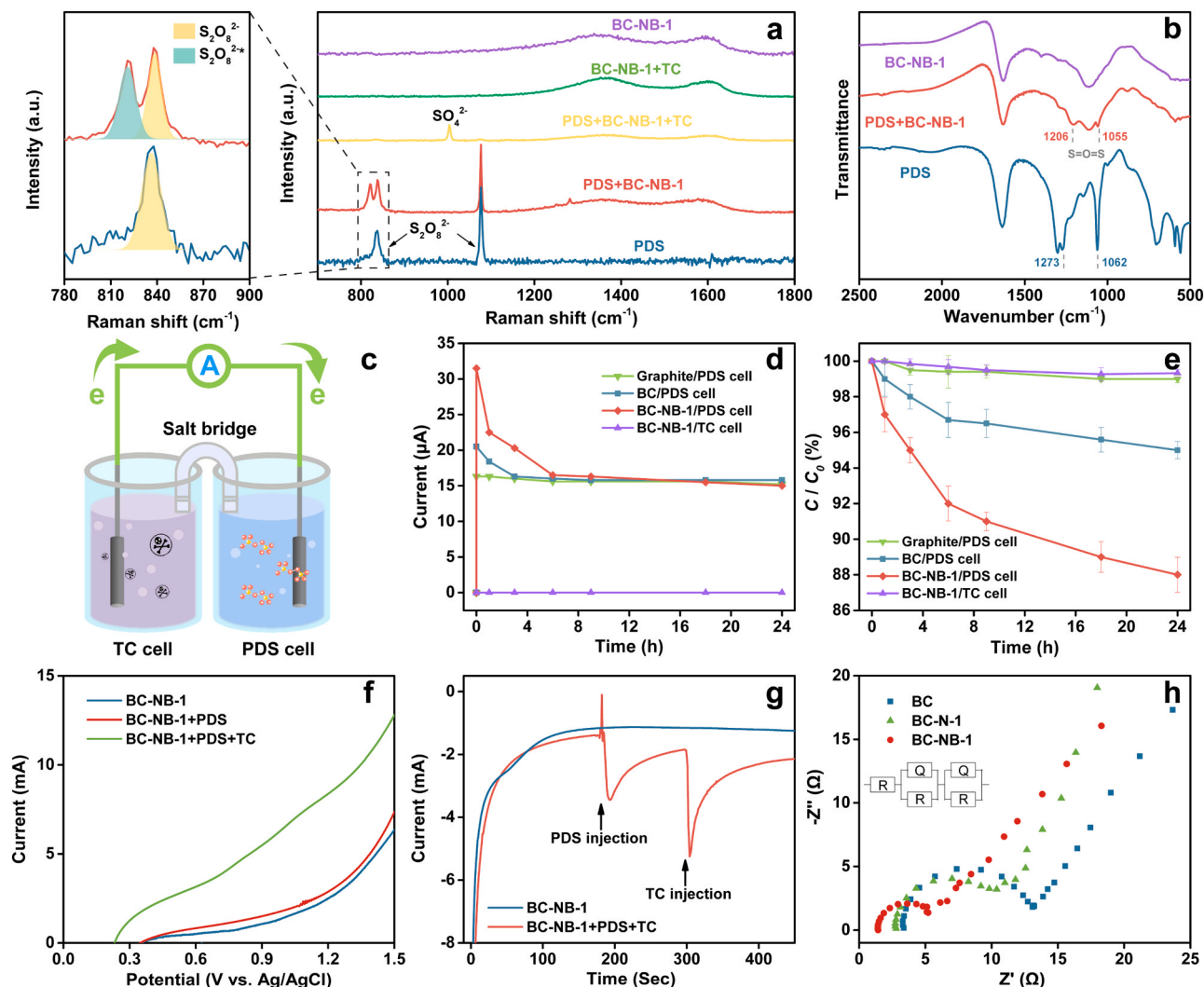
**Fig. 3.** (a) *In situ* Raman spectra; (b) ATR-FTTR spectra; (c) two-chamber galvanic oxidation reactors; (d) current flowing from the TC cell to the PDS cell; (e) TC degradation in the galvanic oxidation reactors; (f) Linear sweep voltammetry, (g) chronoamperometric curves, and (h) EIS Nyquist plots.

### 3.2. PDS activation by different biochars

As shown in Fig. 2a, negligible TC removal was found with PDS alone, while nearly 37% TC removal was achieved when PDS was combined with the pristine biochar. Elevating the N-doping level resulted in the higher catalytic activity of modified biochars, and interestingly, the subsequent B-doping at a minor level induced remarkable performance enhancements, demonstrating that the introduction of dopants was active in improving PDS activation. Associated with the characterization results of biochars, it can be inferred that the excellent catalytic performance of N/B co-doped biochar is probably related to their high specific surface areas, high defect sites, and abundant N/B-dopants. The structural origin of the superior activity of doped biochars was analyzed in detail in Section 3.4. Moreover, less than 20% of TC was adsorbed by all biochars (Fig. S3a), indicating that the removal of TC was mainly attributed to the enhanced catalytic oxidation. Given that the highest degradation performance, BC-NB-1 was applied for further investigation in the following experiments.

### 3.3. Identification of ROS

In previous studies, $SO_4^{\bullet-}$ and $^{\bullet}OH$ were generally considered as typical free radicals during PDS activation [28,29]. Herein, MeOH was chosen as the scavenger to probe the existence of $SO_4^{\bullet-}$ and $^{\bullet}OH$

$(k_{[SO_4^{\bullet-}]} = 1.1 \times 10^7 \ M^{-1} \ s^{-1}$, $k_{[\bullet OH]} = 9.7 \times 10^8 \ M^{-1} \ s^{-1})$, while TBA was used to quench $^{\bullet}OH$ $(k_{[SO_4^{\bullet-}]} = 8.4 \times 10^5 \ M^{-1} \ s^{-1}$, $k_{[\bullet OH]} = 6 \times 10^8 \ M^{-1} \ s^{-1})$ [19,30]. After adding an excess amount of MeOH or TBA (1000-fold), the removal efficiencies of TC decreased by 15.6% and 9.8%, respectively (Fig. 2b). This indirectly suggested that both $SO_4^{\bullet-}$ and $^{\bullet}OH$ probably exist in the system, and $^{\bullet}OH$ was a more dominant free radical. Intriguingly, no EPR signals of DMPO-OH and DMPO-SO$_4^-$ adducts were detected in the BC-NB-1/PDS system, instead, a heptet signal corresponding to 5, 5-dimethylpyrroline-(2)-oxyl-(1) (DMPOX) was observed, and the signal intensity decreased slightly along with the time extension (Fig. 2c) [31,32]. The same signal also appeared after adding TC, and its intensity gradually attenuated due to the consumption by TC oxidation (Fig. S4a). Different mechanisms have been proposed to explain the formation of DMPOX: (1) the rapid transformation of unstable DMPO-SO$_4^-$ adducts (Eq. (12)) [33], and (2) directly oxidized by $^1O_2$ and metastable complexes [34].

$$DMPO + SO_4^{\bullet-} \ \longrightarrow \ DMPO - SO_4^- \ \longrightarrow DMPO - OH \tag{12}$$
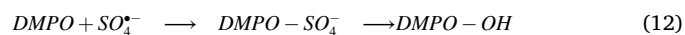
To discern whether $^1O_2$ was produced in the BC-NB-1/PDS system, FFA was selected as the chemical probe [35]. As shown in Fig. 2b, the addition of FFA showed a minor influence (5.7%) on the removal efficiency of TC, implying the possible existence of $^1O_2$. Moreover, a typical TEMP-$^1O_2$ peak was detected in the PDS solution due to the self-decomposition of PDS (Fig. 2d). However, the intensity of the

three-line signal slightly attenuated after the addition of BC-NB-1. This was probably because the adsorption of PDS by BC-NB-1 slow down its reaction with TEMP [12,36]. Assuming that $^1O_2$ was the dominating reactive species, the oxidative efficacy of PDS alone should be higher than that of the BC-NB-1/PDS system due to the higher yield of $^1O_2$. Secondly, if $^1O_2$ is involved in the oxidation, alkaline conditions should promote the removal efficiency because TC would convert into more electron-rich species, which was not the case in our study (Fig. 6b). Thirdly, the addition of TC in PDS/BC-NB-1 suspension did not cause an obvious change in TEMP-$^1O_2$ intensity (Fig. S4b). Finally, previous studies reported that the lifetime of $^1O_2$ in $D_2O$ is ~15 times longer than in $H_2O$, thus the signal of TEMP-$^1O_2$ should be theoretically enhanced in $D_2O$ [37]. However, no remarkable changes in the intensity of TEMP-$^1O_2$ occurred when $H_2O$ was replaced by $D_2O$ (Fig. 2d). Therefore, the inhibitory effect of FFA may be due to its hydrophobic nature, which hinders the adsorption of PDS and TC onto the surface of the biochar, rather than $^1O_2$ quenching [38]. Collectively, it can be inferred that $^1O_2$ made an insignificant contribution to the oxidation of TC. Meanwhile, the possibility of the DMPOX formation caused by $^1O_2$ was also ruled out.

$O_2^{•-}$ has been reported to be an intermediate radical during persulfate activation [39]. As shown in Fig. 2b, the addition of 20 mM p-BQ reduced TC degradation by 11.7%, suggesting $O_2^{•-}$ may be generated. To eliminate interference from $SO_4^{•-}$ and $^•OH$, the EPR detection of $O_2^{•-}$ was conducted in pure MeOH. However, only the signal of DMPOX rather than the DMPO-$O_2^{•-}$ was observed in the BC-NB-1/PDS system (Fig. 2e). A similar scenario was also observed in N-doped porous carbon/PDS systems [38]. To discern the role of $O_2^{•-}$, additional quenching experiments were performed in the $N_2$ atmosphere. It has been reported that $O_2^{•-}$ could be produced from dissolved oxygen through acquiring electrons from catalysts. However, no obvious change was observed in TC degradation after $N_2$ and air purging, implying that dissolved oxygen played a negligible role in producing $O_2^{•-}$ (Fig. S3b). Therefore, $O_2^{•-}$ acts only as an intermediate species but does not account for the TC oxidation given that the redox potential is low ($-0.33$ $V_{NHE}$) [40].

Note that most of TC could still be degraded even if the quencher is excessive, we envisage that another nonradical pathway exists in the BC-NB-1/PDS system yet, which might also be responsible for the DMPOX generation. To distinguish the contributions of radical and nonradical oxidations, competition kinetics experiments were conducted in a mixed system using NB and BA as probe compounds [41]. Combined the reported rate constants of radicals (Table S2) and the experimental results (Fig. S5), the steady-state concentrations of $^•OH$ and $SO_4^{•-}$ in the BC-NB-1/PDS system were calculated to be $1.77 \times 10^{-13}$ and $2.01 \times 10^{-12}$ M, which were higher than those in the pristine BC/PDS system ($^•OH$: $1.09 \times 10^{-13}$ M; $SO_4^{•-}$: $1.05 \times 10^{-12}$ M) and BC-NB-1/PDS system ($^•OH$: $1.56 \times 10^{-13}$ M; $SO_4^{•-}$: $1.29 \times 10^{-12}$ M), respectively. This is probably because doped biochars could donate delocalized electrons to persulfate for the radical generation to some degree owing to rich catalytic sites such as defects and N species [1,10]. Significantly, doped N/B atoms promoted nonradical oxidation to a larger extent. The relative contributions of $^•OH$, $SO_4^{•-}$, and nonradical pathway for TC oxidation in the BC-NB-1/PDS system were estimated to be 28%, 13%, and 59%, indicating the dominant position of nonradical oxidation. For the pristine BC/PDS and BC-N-1/PDS systems, the contributions of nonradical oxidations accounted for just 22% and 32%, respectively (Fig. 2f). This enhanced nonradical contribution was further validated by TCP degradation (from 35% to 64%), which further suggests that the incorporation of heteroatom could enhance more vigorously the nonradical pathway. Additionally, we conducted DMPO-trapping experiments in the BC-N-1/PDS system and found that the signal intensity of DMPOX was much lower than that of the BC-NB-1/PDS system (Fig. 2c), verifying once again a more significant role contributed from nonradical oxidations in the BC-NB-1/PDS system. These results collectively demonstrated that the doping of N and B not only boosted the catalytic performance of biochars but also encouraged

the nonradical pathway and switched the process of PDS activation from a radical manner to a nonradical manner.

## 3.4. Electron-transfer pathway

Previous studies have reported carbon materials could catalyze persulfate to form surface-confined intermediates, and then react with the organics by the mediated electron-transfer regime without producing free radicals [2,42]. We conducted in situ Raman and ATR-FTIR experiments to unveil whether the aforementioned surface-confined species exist. As shown in Fig. 3a, in addition to the peaks of $S_2O_8^{2-}$ at 837 and 1076 cm$^{-1}$, a new peak centered at 820 cm$^{-1}$, originating from the vibration of prolonged O-O bonds (denoted as $S_2O_8^{2-}*$), emerged in the BC-NB-1/PDS system [43]. Subsequently, upon the addition of TC, the peaks of $S_2O_8^{2-}$ and $S_2O_8^{2-}*$ almost disappeared and another peak of $SO_4^{2-}$ arose at 1003 cm$^{-1}$. Accordingly, it is speculated that the emerging $S_2O_8^{2-}*$ can be ascribed to the formation of metastable catalyst/PDS* complexes, which were subsequently consumed by TC via an electron-transfer pathway. During this process, the activated $S_2O_8^{2-}*$ complexes with prolonged O-O bonds present a higher electron-withdrawing activity from TC, resulting in the cleavage of O-O bonds into $SO_4^{2-}$. The FTIR spectrum of PDS alone in Fig. 3b displayed significant characteristic peaks at 1273 and 1062 cm$^{-1}$ (the symmetric and asymmetric vibrations of S=O=S) [44]. Of note, there was a red-shift of 67 and 7 for both peaks when BC-NB-1 was mixed with PDS. This result indicated that the electron density of the S=O=S bond is weakened when PDS is bonded to the surface of biochars, and therefore the formation of a complex between adsorbed PDS molecule and BC-NB-1 might be involved [45].

If such the electron-transfer pathway existed, the addition of TC (electron donor) would promote the decomposition of PDS (electron acceptor) to generate more $SO_4^{2-}$ [42]. As expected, the concentration of $SO_4^{2-}$ increased upon the addition of TC (Fig. S6). This result confirmed again that TC indeed acted as electron donors to facilitate the decomposition of PDS.

To prove this mechanism, a galvanic oxidation reactor was developed to separate PDS and TC into two half cells, so that TC can only be oxidized via an electron-transfer pathway (Fig. 3c). The current and degradation efficiencies of TC were monitored during the reaction. As depicted in Fig. 3d and e, although the graphite electrode without the catalyst coating exhibited a certain current intensity, it did not cause significant degradation of TC. A similar phenomenon was previously observed in the PMS/bisphenol A system [46]. Possible reasons might lie in the weak interaction of graphite with PDS made it difficult to form surface-confined intermediates for shuttling electrons. However, when the graphite electrode coated with BC-NB-1 was applied, a large increase in the current was recorded, and the current value quickly reached the maximum (31.5 μA) and then gradually declined throughout the reaction. This agreed well with the competition kinetics experiments that the N/B doping enhanced the nonradical electron-transfer pathway. Meanwhile, TC in the BC-NB-1/PDS system decomposed at a much faster rate than in the pristine BC/PDS system, indicating that TC was oxidized by direct electron transfer and BC-NB-1 effectively promoted the electrons flowing from the TC cell to the PDS cell. As a control, the BC-NB-1 wrapped graphite electrode was applied in the TC cell. Interestingly, no current and TC degradation was observed, suggesting the key role of the interaction between BC-NB-1 and PDS. This gave strong evidence that TC donated electrons to PDS through BC-NB-1(electron mediator) instead of directly giving PDS electrons.

We further observed a remarkable current increase on the BC-NB-1 wrapped working electrode only when PDS and TC coexisted (Fig. 3f). This scenario suggested that the electron migration from TC to PDS highly relies on the close interaction of both PDS and TC on the BC-NB-1 surface. Chronoamperometric curves more clearly illustrate this current response (Fig. 3g). After the injection of PDS, a distinct positive current flow emerged promptly, witnessing the electron transportation from the
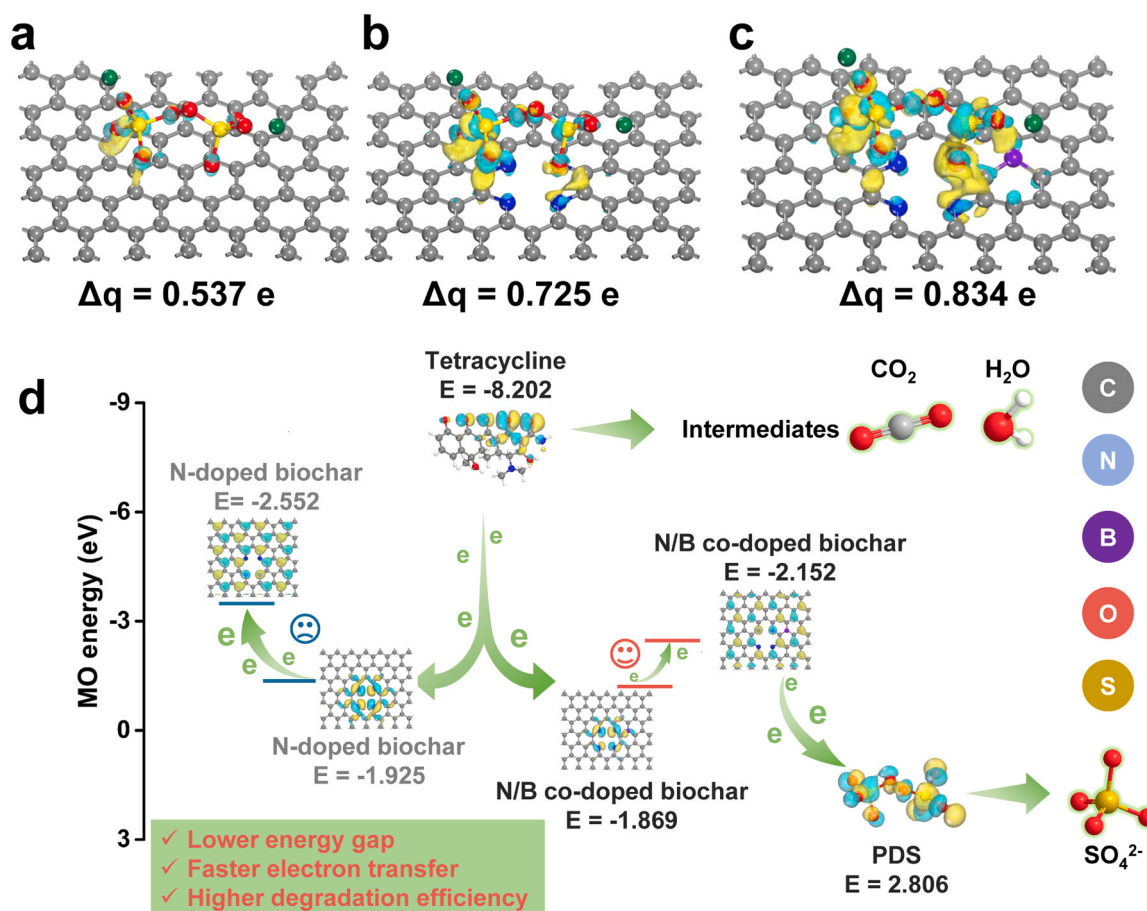
**Fig. 4.** The adsorption of PDS on the (a) pristine biochar, (b) N-doped biochar, and (c) N/B co-doped biochars and the corresponding electron transfer number; (d) electron-transfer pathways driven by potential energy difference for TC oxidation.

BC-NB-1 wrapped electrode to PDS likely through the formation of surface-confined intermediates. The subsequent addition of TC triggered a negative current peak, implying that TC delivered electrons to the BC-NB-1 surface. These results collectively suggested that BC-NB-1 acted as an ''electron bridge'' to facilitate electrons migrate from TC to the metastable BC/PDS* complex, rather than just a catalyst for radicals generation. To support this hypothesis, the electrical property of prepared biochars was investigated by EIS. The Nyquist plot of BC-NB-1 showed a smaller semicircle diameter compared to that of the pristine biochar and BC-N-1, representing the lower electron-transfer resistance (Fig. 3h). Moreover, the decrease of electrical resistivity was further confirmed by the downshift of the G band in N/B co-doping biochars (Fig. 1e) [47]. Previous studies showed that the N doping brings about free electrons while the B doping introduces holes to the graphene sheets, and both of which could promote the transfer of electrons between valence electrons and the conduction band [47]. Therefore, it is reasonable to argue that the synergistic effect of N and B atoms altered the electronic structure of biochars, enabling the carbon matrix more conducive to participate in the electron-transfer process.

To further clarify the origin of superior activities, the structural parameters, including defect degree (Fig. 1e) and specific surface area ($S_{BET}$, Fig. 1f) of biochars were measured and correlated with the values of $k_{obs}$ (Fig. S7a). As shown, N/B co-doping increased the $S_{BET}$ of the pristine biochar, which has a certain role in enhancing the activity of biochars due to the generation of more catalytic sites (Fig. S7b). However, BC-NB-1 manifests a medium $S_{BET}$ (45 m$^2$ g$^{-1}$) but the highest $k_{obs}$, suggesting that $S_{BET}$ is not the decisive factor for the reaction rate. Similarly, the increase in the defect degree, that is, the intensity ratio ($I_D/I_G$) of D (~1329 cm$^{-1}$) and G (~1596 cm$^{-1}$) bands, did not bring

about a continuous increase in the $k_{obs}$ values (Fig. S7c) [48]. It is suggested that defects with a localized region enable their π electrons not to be confined by the conjugated network, herein boosting the high surface adsorption activity and functionality as active sites for charge mobility [49]. However, excessive defective motifs would deteriorate the structural integrity of the conjugated π system, resulting in poor electrical conductivity [50,51]. Therefore, defective sites are not the dominant catalytic centers as well.

The surface oxygen species are recently believed to play a crucial part in persulfate activation [4]. Therefore, we explored the changes in the surface functional groups of fresh and used catalysts by XPS. As indicated, a decrease in the content of C-OH and a simultaneous increase corresponding to C=O bonds were observed in the C 1s and O 1s XPS spectra of BC-NB-1 after the catalytic reaction, suggesting that a part of C-OH groups might be oxidized to C=O groups (Fig. S8 a, b). It was reported that C-OH groups could be converted into organic radicals by releasing protons, which further induce the generation of $SO_4^{\bullet-}$ (Eq. (13)) [51]. Therefore, we speculate that C-OH groups probably participated in the free radical PDS-activated process.

$$BC \quad surface - OH + S_2O_8^{2-} \quad \longrightarrow \quad SO_4^{\bullet-} + BC \quad surface - O^{\bullet} + HSO_4^-$$

(13)
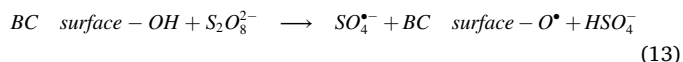
Additionally, we also found a slight decline in the contents of N and B after 4 cycling tests, from 10.22, 1.80–9.43, and 0.95 at%, respectively, which ultimately lead to a decrease in TC degradation (Table 1, Fig. S8e, f). Next, we studied the configurations of N and B in different biochars. Three N bonding configurations including pyridinic N (398.9 eV), pyrrolic N (399.9 eV), and graphitic N (401.2 eV) were fitted in the N 1s spectra (Fig. S9a, b) [34,52]. And as for B 1s spectra, three peaks were
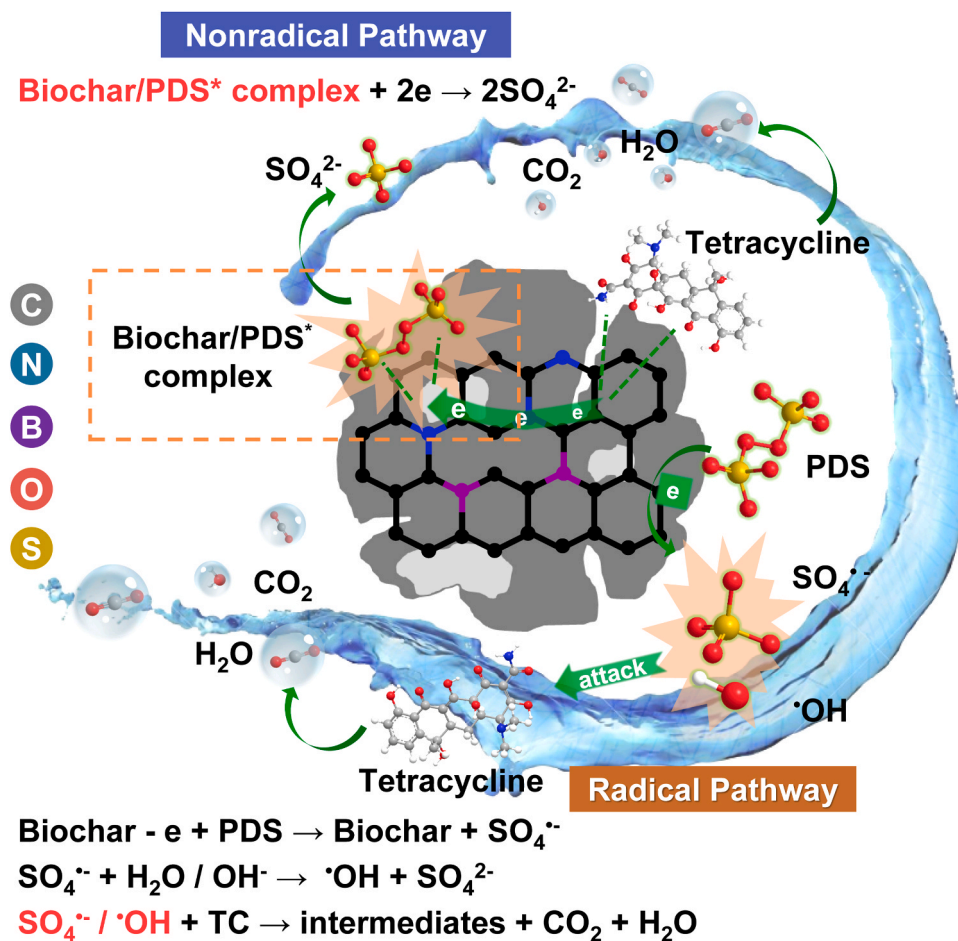
**Fig. 5.** Proposed mechanisms of TC oxidation in the N/B co-doped biochars/PDS system.

identified in the N/B co-doped biochars, corresponding to BC₃ (189.5 eV, each boron bonded with three carbon atoms), BC₂O (190.8 eV, each boron bonded with two carbon atoms and one oxygen atom), and BCO₂ (191.7 eV, each boron bonded with one carbon atom and two oxygen atoms), respectively (Fig. S9c), and this was in agreement with previous reports [6,12]. Among the different N and B configurations, the relative content of pyridinic N and BC₃ showed a positive correlation with $k_{obs}$ (Fig. S7 d–f). These results indicated that doped heteroatoms, especially pyridinic N and BC₃ species, played critical roles in PDS activation. After thermal treatment, the contents N and B species of the BC-NB-1 increased to 9.89 and 1.84 at%, respectively (Table 1), which were comparable to those of the fresh one. And meanwhile, the reclaimed BC-NB-1 recovered most of its catalytic properties (discussed in Section 3.6), reconfirming that the enhanced activity is highly relevant to the incorporated heteroatoms.

### 3.5. Theoretical calculations

Density functional theory calculations were further carried out to unveil the mechanistic roles of dopants in the persulfate-activated process. The optimized configurations and corresponding densities of states (DOSs) for the pristine and doped biochars are displayed in Fig. S10. The result showed that, compared with the pristine biochar, the Fermi level ($E_f$) shifts upward upon co-doping of N and B atoms, implying that the electrons could be transferred more easily in the doped biochars [49]. Meanwhile, as evidenced from Fig. S11, N/B co-doped biochar exhibited a narrower energy gap as compared to that of N-doped one. These findings collectively indicated that the co-doping of N and B in biochars can dramatically improve catalytic activity by reducing the energy

barrier.

Furthermore, as shown in Fig. 4a–c, the number of electron transfers from N/B co-doped biochars to PDS is calculated as 0.834 e, which is higher than those of the pristine biochar (0.537 e) and N-doped biochars (0.725 e), further confirming that the N/B co-doped biochars can readily facilitate the electron transfer from TC to PDS and eventually result in PDS decomposition and TC oxidation.

Based on these discoveries, both radical and nonradical pathways existed during PDS activation while the latter played a more prominent role in TC degradation. Delocalized π electrons from defective sites and lone-pair electrons from functional groups (especially C-OH), pyridinic N, and pyrrolic N of N/B co-doped biochars can be delivered to PDS for evolving $SO_4^{\bullet-}$. Meanwhile, $SO_4^{\bullet-}$ could react with $H_2O$ or $OH^-$ to form $^{\bullet}OH$ radicals. For the nonradical oxidation, the formation of metastable PDS* intermediates on the surface of N/B co-doped biochars was the key to such a process. N/B co-doped biochars could work as the conductive bridge to boost the electron migration from the electron donor (TC) to the electron acceptor (surface-confined BC/PDS* complexes) without generating free radicals. Benefiting from the narrowest energy gap of N/B co-doped biochars, the electrons localized at the highest occupied molecular orbital (HOMO, −8.202 eV) of TC can be readily transferred to the lowest unoccupied molecular orbital (LUMO, 2.806 eV) of metastable PDS* reactive complex via the carbon tunnel driven by a potential energy difference, eventually triggering PDS decomposition (Fig. 4d). During this process, PDS abstracts two electrons from TC, instead of acts as a one-electron oxidant to generate $SO_4^{\bullet-}$. Combining the above analysis, a possible mechanism of TC oxidation in the N/B co-doped biochars/PDS system is proposed in Fig. 5.

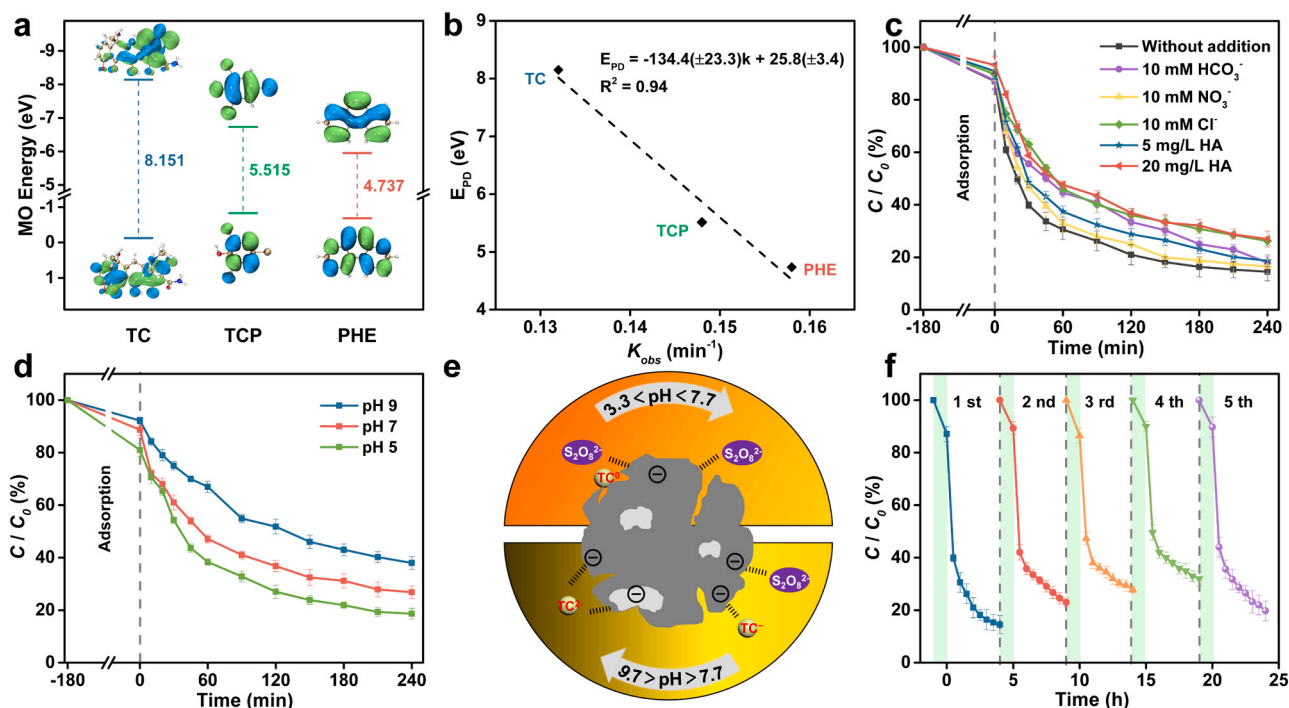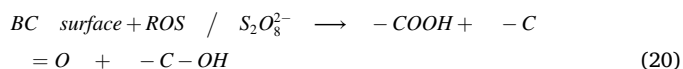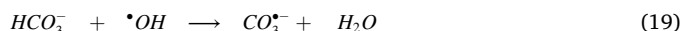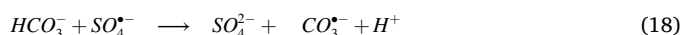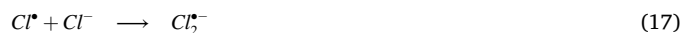To validate this potential energy difference-driven electron transfer

**Fig. 6.** (a) HOMO and LUMO energy levels as well as potential differences of pollutants; (b) correlation between EPD and corresponding $k_{obs}$. Effects of (c) water matrices and (d) solution pH on the degradation of TC in the BC-NB-1/PDS system; (c) schematic of the interaction between biochars, PDS and TC in different pH conditions; (d) reusability experiments.

pathway, two typical organic pollutants (TCP, PHE) were selected, and the corresponding reactivities were investigated in the BC-NB-1/PDS system (Fig. S12). The selected compounds with different molecular structures exhibited distinct disparity in the HOMO-LUMO energy levels as well as potential differences ($E_{PD}$) (Fig. 6a). Meanwhile, the $k_{obs}$ constants of the compounds varied considerably (Fig. 6b). Intriguingly, there was a strong negative correlation between the $k_{obs}$ and $E_{PD}$, implying that the degradation of organics in biochar/PDS systems is highly dependent on $E_{PD}$. The above results not only consolidate the proposed mechanism of potential energy difference-driven electron transfer but also clarify the origin of catalytic activity of heteroatoms doping.

## 3.6. Catalytic performance evaluation

Bearing the feature of the enhanced nonradical oxidation in mind, we further performed degradation experiments under various conditions to evaluate the advantages of the N/B co-doped biochar/PDS system. Radical scavenging by background constituents such as anions and natural organic matter (e.g., humic acid) is a common challenge encountered in $SO_4^{\bullet-}$-based systems. Encouragingly, the TC degradation was less affected by various anions (Fig. 6c). For instance, $Cl^-$ can be oxidized by $SO_4^{\bullet-}$ and $^{\bullet}OH$ to form a suite of chlorine radicals (e.g., $Cl^{\bullet}$ and $ClOH^{\bullet-}$). The kinetics of these chlorine species that react with most organic pollutants are higher than for $SO_4^{\bullet-}$ and $^{\bullet}OH$ but with relatively low standard reduction potentials ($E^0$ ($Cl^{\bullet}/Cl^-$) = 2.4 $V_{NHE}$; $E^0$ ($ClOH^{\bullet-}/Cl^-$) = 1.3 $V_{NHE}$), thus retarding the treatment efficiency [53]. For the same reason, $SO_4^{\bullet-}$ and $^{\bullet}OH$ add to $HCO_3^-$ would form $CO_3^{\bullet-}$ with low reactivity ($E^0$ ($CO_3^{\bullet-}/CO_3^{2-}$) = 1.57 $V_{NHE}$) [54]. Consequently, the oxidation performance tends to decrease. Although $Cl^-$ and $HCO_3^-$ exhibited a relatively high radical scavenging effect compared to $NO_3^-$ (Eqs. (14–19)) [55], the TC removal still achieved a high level, demonstrating the dominance of nonradicals in this system. Unfavorably, the increased dosage of humic acid from 5 to 20 mg $L^{-1}$ leads to a gradual decrease in the degradation efficiency of TC (Fig. 6c). Excessive

humic acid will not only consume the nonselective radicals but compete for the adsorptive sites with PDS and TC, impeding the formation of the surface reactive complex [56].

$$Cl^- + SO_4^{\bullet-} \longrightarrow Cl^{\bullet} + SO_4^{2-} \qquad (14)$$

$$Cl^- + {}^{\bullet}OH \longrightarrow ClOH^{\bullet-} \qquad (15)$$

$$ClOH^{\bullet-} + H^+ \longrightarrow Cl^{\bullet} + H_2O \qquad (16)$$

$$Cl^{\bullet} + Cl^- \longrightarrow Cl_2^{\bullet-} \qquad (17)$$

$$HCO_3^- + SO_4^{\bullet-} \longrightarrow SO_4^{2-} + CO_3^{\bullet-} + H^+ \qquad (18)$$

$$HCO_3^- + {}^{\bullet}OH \longrightarrow CO_3^{\bullet-} + H_2O \qquad (19)$$

$$BC \ surface + ROS \ / \ S_2O_8^{2-} \longrightarrow -COOH + -C$$
$$= O + -C-OH \qquad (20)$$

In addition, the performance of the BC-NB-1/PDS system is strongly correlated with solution pH. From Fig. 6d, the removal efficiency of TC followed the order of pH 5.0 > pH 7.0 > pH 9.0. The lower TC removal at neutral and alkaline pH can be explained by the fact that the surface of BC-NB-1 became more negatively charged, consequently resulting in an increasing electrostatic repulsion among the BC-NB-1 ($pH_{zpc}$ = 3.0, Fig. S13a), deprotonated TC (TC$^-$, TC$^{2-}$, Fig. S13b), and $S_2O_8^{2-}$ (Fig. 6e) [57]. These results proved again the interfacial reaction of active complexes is an essential step for the subsequent oxidation.

We also evaluated the reusability and stability of BC-NB-1 catalysts. As shown, the reused BC-NB-1 induced a continuous decrease in the degradation of TC after each cycle (Fig. 6f). This reduction was probably attributed to the coverage of active sites by the degradation intermediates, which was evidenced by the visible decrease in the contents of N and B (Table 1). Additionally, the surface oxidization caused by ROS/$S_2O_8^{2-}$ (Eq. (20)), as confirmed by the increased O content (from 12.84 to 22.47 at%, Table 1), would not only impair the conductivity of

**Table 2**
Comparison of catalytic performance of different catalyst/persulfate systems.

| Catalyst | Degradation efficiency (%) | TOC removal (%) | Experimental conditions | | | | References |
|---|---|---|---|---|---|---|---|
| | | | PDS (mM) | Catalyst (g/L) | TC (mg/L) | pH | |
| OBC-Fe$_3$O$_4$ | 80.3 | 40.2 | 10 | 0.4 | 20 | 3 | [59] |
| MnFe$_2$O$_4$ | 86.23 | – | 2 | 0.2 | 25 | 4.5 | [60] |
| NiFe$_2$O$_4$ | 80 | – | 0.05 | 0.3 | 20 | 7 | [61] |
| Activated carbon@Fe$_3$O$_4$ | 80.77 | 50.65 | 30 | 0.2 | 30 | 5.5 | [62] |
| Cu-FeOOH/BC | 91.7 | 46.5 | 20 | 0.1 | 20 | 7 | [63] |
| BC-NB-1 | 85.5 | 55 | 1 | 0.2 | 30 | 4.5 | This work |

catalysts but also hinder the interaction between catalysts and PDS due to the stereo-hindrance effect. To verify this argument, the used BC-NB-1 was subjected to annealing at 200 °C for 1 h, in an attempt to remove organic intermediates and excess functional groups [3,58]. XPS analyses confirmed the significant decrease in the O content of biochars after heat treatment due to the decomposition of surface residual organics (Table 1). As shown, the regenerated biochars exhibited a comparable performance as compared with the fresh one, demonstrating that a simple thermal treatment could recover the reactivity of BC-NB-1 (Fig. 6f). Considering the complexity of the real environment, therefore, catalytic experiments were conducted in different water bodies. Compared with that in ultrapure water and tap water, the removal rate of TC was slightly retarded in the artificial surface water due to the integrated effects of competitive adsorptions and radical quenching by anions and natural organic matters (Fig. S13c). Impressively, as high as 74.6% of TC can be eliminated in the realistic wastewater sample, reflecting the practicability of the BC-NB-1/PDS system. In addition to excellent stability, the BC-NB-1/PDS system presented superior mineralization efficiencies (Fig. S13d, 55% TOC removal) towards TC, out-performing reported popular metal oxides, and carbon-catalyzed persulfate systems (Table 2). Collectively, relying on this enhanced nonradical pathway, the N/B co-doped biochar/PDS system exhibited higher reactivity and stability.

## 4. Conclusions

In this work, we reported the doped N and B atoms not only enhanced the catalytic performance of biochars towards PDS activation but effectively encourage the nonradical pathway, resulting in the conversion of the oxidation mechanism from a classic radical process to a nonradical process. Compared with SO$_4^{\bullet-}$ and $^{\bullet}$OH radicals, a mediated electron-transfer pathway made a greater contribution to TC oxidation, which made the N/B co-doped biochar/PDS system exhibited significant resistance against common species in environments. Despite high surface areas and defective levels have a certain role in enhancing the activity of biochars, they are not the decisive factors. N and B doping synergistically accelerated the electron transfer from the HOMO of adsorbed TC to the LUMO of metastable biochar/PDS complexes via the conductive carbon tunnel, eventually resulting in TC decomposition, in which pyridinic N and BC$_3$ configurations may be the essential active sites. Benefiting from its low price and simple preparation process, the metal-free doped biochar is ideally suited for the actual wastewater treatment. These findings provided a novel and feasible approach for the rational design of reaction-targeted carbocatalysts for persulfate activation, more importantly, shed new light on the critical roles of heteroatoms in mediated electron-transfer pathways.

## CRediT authorship contribution statement

**Jibo Dou**: Conceptualization, Methodology, Software, Visualization, Investigation, Writing – original draft. **Jie Cheng**: Investigation, Validation. **Zhijiang Lu**: Investigation, Validation. **Ziqi Tian**: Formal analysis, Resources. **Jianming Xu**: Writing – review & editing, Supervision. **Yan He**: Conceptualization, Methodology, Supervision, Writing – review & editing, Project administration, Funding acquisition.

## Declaration of Competing Interest

The authors declare that they have no known competing financial interests or personal relationships that could have appeared to influence the work reported in this paper.

## Acknowledgments

## Appendix A. Supplementary data

Characterizations of biochars, kinetics calculation, galvanic oxidation reactor, pollutant quantification, EPR measurements, electrochemical tests, in situ Raman, theoretical calculations (Text S1–S8); the compositions of artificial surface water and wastewater, second-order rate constants of radicals (Tables S1,S2); XPS spectra, TC adsorption, purging N$_2$ experiments, competition experiments, kinetic constants, computational results, the zeta potential of BC-NB-1, and TOC removal (Figs. S1–S13).

## Appendix B. Supporting information

Supplementary data associated with this article can be found in the online version at doi:10.1016/j.apcatb.2021.120832.

## References

[1] X. Chen, W. Oh, Z. Hu, Y. Sun, R. Webster, S. Li, T. Lim, Enhancing sulfacetamide degradation by peroxymonosulfate activation with N-doped graphene produced through delicately-controlled nitrogen functionalization via tweaking thermal annealing processes, Appl. Catal. B Environ. 225 (2018) 243–257, https://doi.org/10.1016/j.apcatb.2017.11.071.

[2] W. Ren, G. Nie, P. Zhou, H. Zhang, X. Duan, S. Wang, The intrinsic nature of persulfate activation and N-doping in carbocatalysis, Environ. Sci. Technol. 54 (2020) 6438–6447, https://doi.org/10.1021/acs.est.0c01161.

[3] P. Hu, H. Su, Z. Chen, C. Yu, Q. Li, B. Zhou, P. Alvarez, M. Long, Selective degradation of organic pollutants using an efficient metal-free catalyst derived from carbonized polypyrrole via peroxymonosulfate activation, Environ. Sci. Technol. 51 (2017) 11288–11296, https://doi.org/10.1021/acs.est.7b03014.

[4] W. Ren, L. Xiong, G. Nie, H. Zhang, X. Duan, S. Wang, Insights into the electron-transfer regime of peroxydisulfate activation on carbon nanotubes: the role of oxygen functional groups, Environ. Sci. Technol. 54 (2020) 1267–1275, https://doi.org/10.1021/acs.est.9b06208.

[5] X. Duan, H. Sun, Y. Wang, J. Kang, S. Wang, N-doping-induced nonradical reaction on single-walled carbon nanotubes for catalytic phenol oxidation, ACS Catal. 5 (2015) 553–559, https://doi.org/10.1021/cs5017613.

[6] B. Liu, W. Guo, H. Wang, Q. Si, Q. Zhao, H. Luo, N. Ren, B-doped graphitic porous biochar with enhanced surface affinity and electron transfer for efficient peroxydisulfate activation, Chem. Eng. J. 396 (2020), 125119, https://doi.org/10.1016/j.cej.2020.125119.

[7] H. Liu, P. Sun, M. Feng, H. Liu, S. Yang, L. Wang, Z. Wang, Nitrogen and sulfur co-doped CNT-COOH as an efficient metal-free catalyst for the degradation of UV filter BP-4 based on sulfate radicals, Appl. Catal. B Environ. 187 (2016) 1–10, https://doi.org/10.1016/j.apcatb.2016.01.036.

[8] G. Fang, C. Liu, J. Gao, D.D. Dionysiou, D. Zhou, Manipulation of persistent free radicals in biochar to activate persulfate for contaminant degradation, Environ. Sci. Technol. 49 (2015) 5645–5653, https://doi.org/10.1021/es5061512.

[9] J. Liang, X. Duan, X. Xu, K. Chen, Y. Zhang, L. Zhao, H. Qiu, S. Wang, X. Cao, Persulfate oxidation of sulfamethoxazole by magnetic iron-char composites via nonradical pathways: Fe (IV) versus surface-mediated electron transfer, Environ. Sci. Technol. 55 (2021) 10077–10086, https://doi.org/10.1021/acs.est.1c01618.

[10] S. Zhu, X. Huang, F. Ma, L. Wang, X. Duan, S. Wang, Catalytic removal of aqueous contaminants on N-doped graphitic biochars: inherent roles of adsorption and nonradical mechanisms, Environ. Sci. Technol. 52 (2018) 8649–8658, https://doi.org/10.1021/acs.est.8b01817.

[11] S.H. Ho, R. Li, C. Zhang, Y. Ge, G. Cao, M. Ma, X. Guang, S. Wang, N. Ren, N-doped graphitic biochars from C-phycocyanin extracted Spirulina residue for catalytic persulfate activation toward nonradical disinfection and organic oxidation, Water Res. 159 (2019) 77–86, https://doi.org/10.1016/j.watres.2019.05.008.

[12] C. Nie, Z. Dai, W. Liu, X. Duan, C. Wang, B. Lai, Z. Ao, S. Wang, T. An, Criteria of active sites in nonradical persulfate activation process from integrated experimental and theoretical investigations: boron-nitrogen-co-doped nanocarbon-mediated peroxydisulfate activation as an example, Environ. Sci. Nano 7 (2020) 1899–1911, https://doi.org/10.1039/D0EN00347F.

[13] C. Chen, D. Yan, Y. Wang, Y. Zhou, Y. Zou, Y. Li, S. Wang, B-N pairs enriched defective carbon nanosheets for ammonia synthesis with high efficiency, Small 15 (2019), 1805029, https://doi.org/10.1002/smll.201805029.

[14] X. Li, X. Huang, S. Xi, S. Miao, J. Ding, W. Cai, S. Liu, X. Yang, H. Yang, J. Gao, J. Wang, Y. Huang, T. Zhang, B. Liu, Single cobalt atoms anchored on porous N-doped graphene with dual reaction sites for efficient Fenton-like catalysis, J. Am. Chem. Soc. 140 (2018) 12469–12475, https://doi.org/10.1021/jacs.8b05992.

[15] J. Wang, L. Chu, L. Wojnárovits, T. Erzsébet, Occurrence and fate of antibiotics, antibiotic resistant genes (ARGs) and antibiotic resistant bacteria (ARB) in municipal wastewater treatment plant: an overview, Sci. Total Environ. 744 (2020), 140997, https://doi.org/10.1016/j.scitotenv.2020.140997.

[16] J. Wang, S. Wang, Activation of persulfate (PS) and peroxymonosulfate (PMS) and application for the degradation of emerging contaminants, Chem. Eng. J. 334 (2018) 1502–1517, https://doi.org/10.1016/j.cej.2017.11.059.

[17] Y. Ji, Y. Shi, W. Dong, X. Wen, M. Jiang, J. Lu, Thermo-activated persulfate oxidation system for tetracycline antibiotics degradation in aqueous solution, Chem. Eng. J. 298 (2016) 225–233, https://doi.org/10.1016/j.cej.2016.04.028.

[18] T. Wu, H. Shen, L. Sun, B. Cheng, B. Liu, J. Shen, Nitrogen and boron doped monolayer graphene by chemical vapor deposition using polystyrene, urea and boric acid, New J. Chem. 36 (2012) 1385–1391, https://doi.org/10.1039/C2NJ40068E.

[19] L. Tang, Y. Liu, J. Wang, G. Zeng, Y. Deng, H. Dong, H. Feng, J. Wang, B. Peng, Enhanced activation process of persulfate by mesoporous carbon for degradation of aqueous organic pollutants: electron transfer mechanism, Appl. Catal. B Environ. 231 (2018) 1–10, https://doi.org/10.1016/j.apcatb.2018.02.059.

[20] G. Kresse, J. Furthmüller, Efficient iterative schemes for ab initio total-energy calculations using a plane-wave basis set, Phys. Rev. B 54 (1996) 11169–11186, https://doi.org/10.1103/PhysRevB.54.11169.

[21] G. Kresse, J. Furthmuller, Efficiency of ab-initio total energy calculations for metals and semiconductors using a plane-wave basis set, Comput. Mater. Sci. 6 (1996) 15–50, https://doi.org/10.1016/0927-0256(96)00008-0.

[22] J.P. Perdew, K. Burke, M. Ernzerhof, Generalized gradient approximation made simple, Phys. Rev. Lett. 77 (1996) 3865–3868, https://doi.org/10.1103/PhysRevLett.77.3865.

[23] W. Humphrey, A. Dalke, K. Schulten, VMD: visual molecular dynamics, J. Mol. Graph. 14 (1996) 33–38, https://doi.org/10.1016/0263-7855(96)00018-5.

[24] T. Lu, F. Chen, Multiwfn: a multifunctional wavefunction analyzer, J. Comput. Chem. 33 (2012) 580–592, https://doi.org/10.1002/jcc.22885.

[25] D. Ding, S. Yang, X. Qian, L. Chen, T. Cai, Nitrogen-doping positively whilst sulfur-doping negatively affect the catalytic activity of biochar for the degradation of organic contaminant, Appl. Catal. B Environ. 263 (2020) 118348, https://doi.org/10.1016/j.apcatb.2019.118348.

[26] X. Chen, X. Duan, W.D. Oh, P. Zhang, C. Guan, Y. Zhu, T. Lim, Insights into nitrogen and boron-co-doped graphene toward high-performance peroxymonosulfate activation: maneuverable NB bonding configurations and oxidation pathways, Appl. Catal. B Environ. 253 (2019) 419–432, https://doi.org/10.1016/j.apcatb.2019.04.018.

[27] D. Lee, B. Lee, K.H. Park, H. Ryu, S. Jeon, S. Hong, Scalable exfoliation process for highly soluble boron nitride nanoplatelets by hydroxide-assisted ball milling, Nano Lett. 15 (2015) 1238–1244, https://doi.org/10.1021/nl504397h.

[28] G.P. Anipsitakis, D.D. Dionysiou, Degradation of organic contaminants in water with sulfate radicals generated by the conjunction of peroxymonosulfate with cobalt, Environ. Sci. Technol. 37 (2003) 4790–4797, https://doi.org/10.1021/es0263792.

[29] J. Lee, U. von Gunten, J.-H. Kim, Persulfate-based advanced oxidation: critical assessment of opportunities and roadblocks, Environ. Sci. Technol. 54 (2020) 3064–3081, https://doi.org/10.1021/acs.est.9b07082.

[30] S. Wang, J. Wang, Nitrogen doping sludge-derived biochar to activate peroxymonosulfate for degradation of sulfamethoxazole: modulation of degradation mechanism by calcination temperature, J. Hazard. Mater. 418 (2021), 126309, https://doi.org/10.1016/j.jhazmat.2021.126309.

[31] M. Mian, G. Liu, B. Fu, Y. Song, Facile synthesis of sludge-derived $MnO_x$-N-biochar as an efficient catalyst for peroxymonosulfate activation, Appl. Catal. B Environ. 255 (2019) 117765, https://doi.org/10.1016/j.apcatb.2019.117765.

[32] C. Sun, T. Chen, Q. Huang, M. Zhan, X. Li, J. Yan, Activation of persulfate by $CO_2$-activated biochar for improved phenolic pollutant degradation: performance and

[33] P. Neta, R.E. Huie, A.B. Ross, Rate constants for reactions of inorganic radicals in aqueous-solution, J. Phys. Chem. Ref. Data 17 (1988) 1027–1284, https://doi.org/10.1063/1.555808.

[34] Y. Zhang, B.-T. Zhang, Y. Teng, J. Zhao, X. Sun, Heterogeneous activation of persulfate by carbon nanofiber supported $Fe_3O_4$@carbon composites for efficient ibuprofen degradation, J. Hazard. Mater. 401 (2021), 123428, https://doi.org/10.1016/j.jhazmat.2020.123428.

[35] E.T. Yun, J.H. Lee, J. Kim, H.D. Park, J. Lee, Identifying the nonradical mechanism in the peroxymonosulfate activation process: singlet oxygenation versus mediated electron transfer, Environ. Sci. Technol. 52 (2018) 7032–7042, https://doi.org/10.1021/acs.est.8b00959.

[36] C. Han, X. Duan, M. Zhang, W. Fu, X. Duan, W. Ma, S. Liu, S. Wang, X. Zhou, Role of electronic properties in partition of radical and nonradical processes of carbocatalysis toward peroxymonosulfate activation, Carbon 153 (2019) 73–80, https://doi.org/10.1016/j.carbon.2019.06.107.

[37] C. Castaño, A.H. Thomas, C. Lorente, Type I photosensitized oxidation of methionine, Photochem. Photobiol. 97 (2021) 91–98, https://doi.org/10.1111/php.13314.

[38] Y. Liu, W. Miao, X. Fang, Y. Tang, D. Wu, S. Mao, MOF-derived metal-free N-doped porous carbon mediated peroxydisulfate activation via radical and non-radical pathways: role of graphitic N and C-O, Chem. Eng. J. 380 (2020), 122584, https://doi.org/10.1016/j.cej.2019.122584.

[39] G. Fang, D. Dionysiou, S. Al-Abed, D. Zhou, Superoxide radical driving the activation of persulfate by magnetite nanoparticles: implications for the degradation of PCBs, Appl. Catal. B Environ. 129 (2013) 325–332, https://doi.org/10.1016/j.apcatb.2012.09.042.

[40] Y. Nosaka, A. Nosaka, Generation and detection of reactive oxygen species in photocatalysis, Chem. Rev. 117 (2017) 11302–11336, https://doi.org/10.1021/acs.chemrev.7b00161.

[41] Z. Wang, G. Chen, S. Patton, C. Ren, J. Liu, H. Liu, Degradation of nitrilotris-methylenephosphonic acid (NTMP) antiscalant via persulfate photolysis: implications on desalination concentrate treatment, Water Res. 159 (2019) 30–37, https://doi.org/10.1016/j.watres.2019.04.051.

[42] H. Wang, W. Guo, B. Liu, Q. Si, H. Luo, Q. Zhao, N. Ren, Sludge-derived biochar as efficient persulfate activators: sulfurization-induced electronic structure modulation and disparate nonradical mechanisms, Appl. Catal. B Environ. 279 (2020), 119361, https://doi.org/10.1016/j.apcatb.2020.119361.

[43] Q. Yang, Y. Chen, X. Duan, S. Zhou, Y. Niu, H. Sun, L. Zhi, S. Wang, Unzipping carbon nanotubes to nanoribbons for revealing the mechanism of nonradical oxidation by carbocatalysis, Appl. Catal. B Environ. 276 (2020), 119146, https://doi.org/10.1016/j.apcatb.2020.119146.

[44] D. Xia, Y. Li, G. Huang, R. Yin, T. An, G. Li, H. Zhao, A. Lu, P. Wong, Activation of persulfates by natural magnetic pyrrhotite for water disinfection: efficiency, mechanisms, and stability, Water Res. 112 (2017) 236–247, https://doi.org/10.1016/j.watres.2017.01.052.

[45] J. Liu, Z. Zhao, P. Shao, F. Cui, Activation of peroxymonosulfate with magnetic $Fe_3O_4$-$MnO_2$ core-shell nanocomposites for 4-chlorophenol degradation, Chem. Eng. J. 262 (2015) 854–861, https://doi.org/10.1016/j.cej.2014.10.043.

[46] K. Huang, H. Zhang, Direct electron-transfer-based peroxymonosulfate activation by iron-doped manganese oxide ($\delta$-$MnO_2$) and the development of galvanic oxidation processes (GOPs), Environ. Sci. Technol. 53 (2019) 12610–12620, https://doi.org/10.1021/acs.est.9b03648.

[47] Q.H. Yang, P.X. Hou, M. Unno, S. Yamauchi, R. Saito, T. Kyotani, Dual Raman features of double coaxial carbon nanotubes with N-doped and B-doped multiwalls, Nano Lett. 5 (2005) 2465–2469, https://doi.org/10.1021/nl051779j.

[48] H. Sun, S. Liu, G. Zhou, H.M. Ang, M.O. Tadé, S. Wang, Reduced graphene oxide for catalytic oxidation of aqueous organic pollutants, ACS Appl. Mater. Interfaces 4 (2012) 5466–5471, https://doi.org/10.1021/am301372d.

[49] P. Shao, S. Yu, X. Duan, L. Yang, H. Shi, L. Ding, J. Tian, L. Yang, X. Luo, S. Wang, Potential difference driving electron transfer via defective carbon nanotubes toward selective oxidation of organic micropollutants, Environ. Sci. Technol. 54 (2020) 8464–8472, https://doi.org/10.1021/acs.est.0c02645.

[50] W. Zhang, J. Zhu, H. Ang, Y. Zeng, N. Xiao, Y. Gao, W. Liu, H.H. Hng, Q. Yan, Binder-free graphene foams for $O_2$ electrodes of $Li$-$O_2$ batteries, Nanoscale 5 (2013) 9651–9658, https://doi.org/10.1039/C3NR03321J.

[51] J. Yan, W. Gao, M. Dong, L. Han, L. Qian, C.P. Nathanail, M. Chen, Degradation of trichloroethylene by activated persulfate using a reduced graphene oxide supported magnetite nanoparticle, Chem. Eng. J. 295 (2016) 309–316, https://doi.org/10.1016/j.cej.2016.01.085.

[52] H. Yan, L. Wang, Y. Chen, L. Jiao, Y. Wu, W. Xu, W. Song, D. Du, C. Zhu, Fine-tuning pyridinic N in nitrogen-doped porous carbon nanostructures for boosted peroxidase-like activity and sensitive biosensing, Research 2020 (2020), 8202584, https://doi.org/10.34133/2020/8202584.

[53] R. Pang, Y. Miseki, S. Okunaka, K. Sayama, Photocatalytic production of hypochlorous acid over $Pt/WO_3$ under simulated solar light, ACS Sustain. Chem. Eng. 8 (2020) 8629–8637, https://doi.org/10.1021/acssuschemeng.0c01341.

[54] S. Zilberg, A. Mizrahi, D. Meyerstein, H. Kornweitz, Carbonate and carbonate anion radicals in aqueous solutions exist as $CO_3(H_2O)_6^{2-}$ and $CO_3(H_2O)_6^{\bullet-}$ respectively: the crucial role of the inner hydration sphere of anions in explaining their properties, Phys. Chem. Chem. Phys. 20 (2018) 9429–9435, https://doi.org/10.1039/C7CP08240A.

[55] R. Luo, M. Li, C. Wang, M. Zhang, M.A.N. Khan, X. Sun, J. Shen, W. Han, L. Wang, J. Li, Singlet oxygen-dominated non-radical oxidation process for efficient

degradation of bisphenol A under high salinity condition, Water Res. 148 (2019) 416–424, https://doi.org/10.1016/j.watres.2018.10.087.

[56] T. Zhang, H. Zhu, J.-P. Croué, Production of sulfate radical from peroxymonosulfate induced by a magnetically separable $CuFe_2O_4$ spinel in water: efficiency, stability, and mechanism, Environ. Sci. Technol. 47 (2013) 2784–2791, https://doi.org/10.1021/es304721g.

[57] P. Zhang, Y. Li, Y. Cao, L. Han, Characteristics of tetracycline adsorption by cow manure biochar prepared at different pyrolysis temperatures, Bioresour. Technol. 285 (2019), 121348, https://doi.org/10.1016/j.biortech.2019.121348.

[58] W. Oh, G. Lisak, R. Webster, T. Liang, A. Veksha, A. Giannis, J. Moo, J. Lim, T. Lim, Insights into the thermolytic transformation of lignocellulosic biomass waste to redox-active carbocatalyst: durability of surface active sites, Appl. Catal. B Environ. 233 (2018) 120–129, https://doi.org/10.1016/j.apcatb.2018.03.106.

[59] Z. Pi, X. Li, D. Wang, Q. Xu, Z. Tao, X. Huang, F. Yao, Y. Wu, L. He, Q. Yang, Persulfate activation by oxidation biochar supported magnetite particles for tetracycline removal: performance and degradation pathway, J. Clean. Prod. 235 (2019) 1103–1115, https://doi.org/10.1016/j.jclepro.2019.07.037.

[60] S. Tang, M. Zhao, D. Yuan, X. Li, X. Zhang, Z. Wang, T. Jiao, K. Wang, $MnFe_2O_4$ nanoparticles promoted electrochemical oxidation coupling with persulfate activation for tetracycline degradation, Sep. Purif. Technol. 255 (2021), 117690, https://doi.org/10.1016/j.seppur.2020.117690.

[61] R. Guan, X. Yuan, Z. Wu, H. Wang, L. Jiang, J. Zhang, Y. Li, G. Zeng, D. Mo, Accelerated tetracycline degradation by persulfate activated with heterogeneous magnetic $NixFe_{3-x}O_4$ catalysts, Chem. Eng. J. 350 (2018) 573–584, https://doi.org/10.1016/j.cej.2018.05.195.

[62] A.J. Jafari, B. Kakavandi, N. Jaafarzadeh, R. Kalantary, M. Ahmadi, A. Babaei, Fenton-like catalytic oxidation of tetracycline by $AC@Fe_3O_4$ as a heterogeneous persulfate activator: adsorption and degradation studies, J. Ind. Eng. Chem. 45 (2017) 323–333, https://doi.org/10.1016/j.jiec.2016.09.044.

[63] J. Xu, X. Zhang, C. Sun, J. Wan, H. He, F. Wang, Y. Dai, S. Yang, Y. Lin, X. Zhan, Insights into removal of tetracycline by persulfate activation with peanut shell biochar coupled with amorphous Cu-doped FeOOH composite in aqueous solution, Environ. Sci. Pollut. Res. 26 (2019) 2820–2834, https://doi.org/10.1007/s11356-018-3777-1.